

Article

Strain Profile in the Subsurface of He-Ion-Irradiated Tungsten Accessed by S-GIXRD

Wenjie Huang^{1,2}, Meng Sun^{1,*} , Wen Wen³, Junfeng Yang^{1,*} , Zhuoming Xie¹, Rui Liu¹, Xianping Wang¹, Xuebang Wu¹ , Qianfeng Fang^{1,*} and Changsong Liu¹

¹ Key Laboratory of Materials Physics, Institute of Solid State Physics, HFIPS, Chinese Academy of Sciences, Hefei 230031, China; 18756993930@163.com (W.H.); zmxie@issp.ac.cn (Z.X.); rui.liu@issp.ac.cn (R.L.); xpwang@issp.ac.cn (X.W.); xbwu@issp.ac.cn (X.W.); cslu@issp.ac.cn (C.L.)

² Department of Materials Science and Engineering, University of Science and Technology of China, Hefei 230026, China

³ Shanghai Advanced Research Institute, Chinese Academy of Sciences, Shanghai 201204, China; wenwen@sinap.ac.cn

* Correspondence: mengsun@issp.ac.cn (M.S.); jfyang@issp.ac.cn (J.Y.); qffang@issp.ac.cn (Q.F.)

Abstract: The strain profile in the subsurface of He-ion-irradiated W was figured out by unfolding the synchrotron-grazing incidence X-ray diffraction (S-GIXRD) patterns at different incidence angles. The results show that for 2×10^{21} ions/m² He²⁺-irradiated W, in addition to a compressive strain exists in the depths of 0–100 nm due to mechanical polishing, an expansion strain appears in the depth beyond 100 nm owing to irradiation-induced lattice swelling. This work provides a reference for the study of irradiation damage in the subsurface by S-GIXRD.

Keywords: nuclear materials; X-ray techniques; helium ion irradiation; strain profile



Citation: Huang, W.; Sun, M.; Wen, W.; Yang, J.; Xie, Z.; Liu, R.; Wang, X.; Wu, X.; Fang, Q.; Liu, C. Strain Profile in the Subsurface of He-Ion-Irradiated Tungsten Accessed by S-GIXRD. *Crystals* **2022**, *12*, 691. <https://doi.org/10.3390/cryst12050691>

Academic Editor: Tomasz Sadowski

Received: 19 April 2022

Accepted: 10 May 2022

Published: 12 May 2022

Publisher's Note: MDPI stays neutral with regard to jurisdictional claims in published maps and institutional affiliations.



Copyright: © 2022 by the authors. Licensee MDPI, Basel, Switzerland. This article is an open access article distributed under the terms and conditions of the Creative Commons Attribution (CC BY) license (<https://creativecommons.org/licenses/by/4.0/>).

1. Introduction

Tungsten is one of the primary candidates for plasma-facing materials (PFMs) in future nuclear fusion reactors [1], where the bombardment of high-flux He ions is inevitable. The effects of He irradiation can cause the swelling, embrittlement, and hardening of W and thus greatly reduce the efficiency and integrity of the component [2–5]. So, it is important to investigate the microstructure evolution in the subsurface of W after He-ion irradiation.

Grazing incidence X-ray diffraction (GIXRD) is sensitive to the strain profile in the subsurface of a metal and has advantages such as a wider detection area and more statistical and reliable results over other microscopic methods such as transmission electron microscopy (TEM) [6–10]. However, in a previous GIXRD study [6], it was found that He⁺-irradiated W samples have a wide strain-distribution gradient from the surface to the interior, which is difficult to unfold using existing XRD analysis software such as MDI Jade, GSAS, and Full-prof, etc. [11–13]. Therefore, the unfolding of GIXRD spectra is a key issue to figure out the microstructure in subsurface of the ion-irradiated W. In this paper, a new method for unfolding GIXRD data is suggested, and the micro-strain distribution in subsurface of He²⁺ irradiated tungsten is evaluated.

2. Experimental Details

The pure tungsten was prepared as in [14] and annealed at 1200 °C in a vacuum (10^{-4} Pa) for 1 h. The microstructure consists of large grains (30 μm) with numerous fine sub-grains (3 μm) inside. The tungsten specimens with a size of $5 \times 5 \times 1$ mm³ were mechanically polished to a mirror-like surface, then electrolytic polished in 5% sodium hydroxide aqueous solution, and finally irradiated at room temperature (RT) using a beam of He²⁺ at 400 keV with a total fluence of 2×10^{21} ions/m² in the Institute of Modern Physics, Chinese Academy of Sciences.

The synchrotron grazing incidence X-ray diffraction (S-GIXRD) was carried out with a wavelength of 0.6877 Å at the BL14B1 diffraction beamline stations at the Shanghai Synchrotron Radiation Facility (SSRF) in Shanghai, China. The penetration depth (D_w) of the X-rays depends on the incident angle (ω) and can be described as [15]:

$$D_w = \frac{\sin\omega}{\mu\rho}, \quad (1)$$

where $\mu = 1561 \text{ cm}^{-1}$ represents the X-ray linear absorption coefficient in tungsten at a photon energy of 18 keV [16]. $\rho = 97.16\%$ is the relative density of the present samples. The incident angles were set to 0.1°, 0.2°, 0.3°, 0.5°, 1°, 1.5°, 2°, 2.5°, 3°, 4°, 5°, 7°, and 10° in this experiment, corresponding to penetration depths of 11, 23, 35, 58, 115, 173, 230, 287, 345, 460, 574, 803, and 1145 nm, respectively.

A pure tungsten specimen irradiated at RT with a fluence of $2 \times 10^{21} \text{ ions/m}^2$ was prepared for transmission electron microscopy analysis (TEM, JEM-2010F, JPN). To observe the microstructure of the irradiation defects at different depths, the samples for TEM were prepared using the Focused Ion Beam (FIB) lift-off technique.

3. Results and Discussion

Figure 1 presents the S-GIXRD patterns near the (110) diffraction peak of the unirradiated sample at incident angles of 0.5°, 1°, and 3°. It can be clearly seen that, at low incident angles of 0.5° and 1°, there is a compression strain induced by the polishing treatment, as reported in [6]. At the incident angle of 3°, the position of the main diffraction peak moves to a lower angle, which corresponds to the (110) interplaner spacing for the unstrained W as shown by the black line. The other diffraction peaks have similar characteristics and are not shown here.

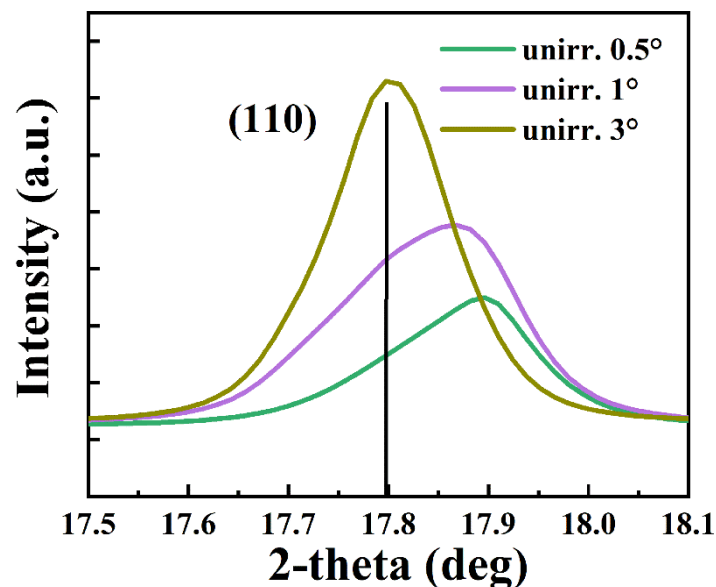


Figure 1. S-GIXRD patterns near the (110) diffraction peak of unirradiated W.

The S-GIXRD patterns for the irradiated W at different incident angles from 0.1° to 10° are shown in Figure 2a. The basic diffraction peaks can be indexed as (110), (200), (211), and (220) of the body-centered cubic structure [6]. The enlarged (110) peaks were given in Figure 2b–d. It can be seen that, with the increasing incident angle, the (110) peak shifts to a lower 2θ angle, and a shoulder peak appears gradually on the left of the peak. The appearance of the shoulder peak means that irradiation-induced lattice swelling exists. In addition, the diffraction peaks of the irradiated samples are more zig-zagged than those of the unirradiated samples, indicating a non-uniform distribution of the (110)

interplaner spacing from the surface to the interior. Therefore, analyzing these S-GIXRD data at different incident angles is crucial to studying the microstructure evolution after ion irradiation.

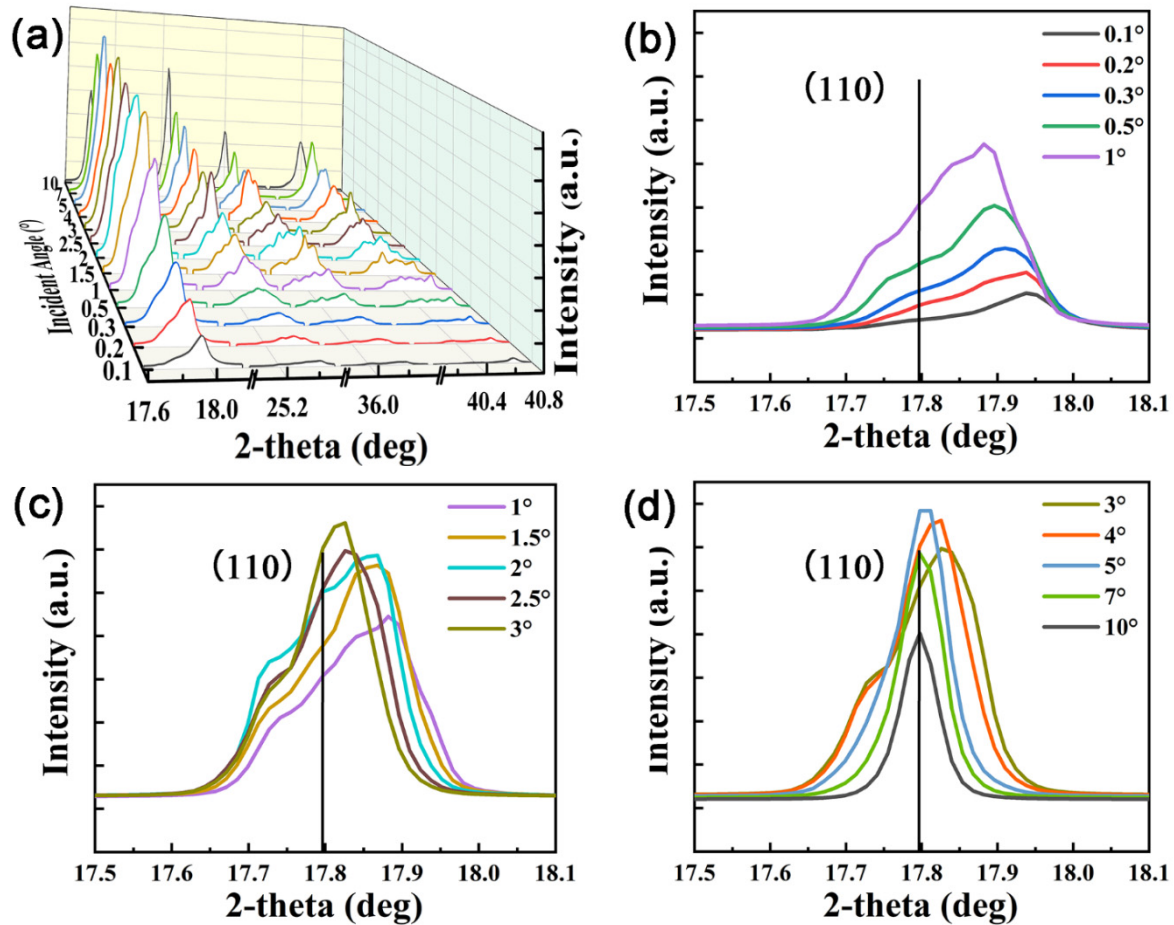


Figure 2. (a) S-GIXRD patterns of 2×10^{21} He ions/ m^2 irradiated W at different incident angles. The enlarged (110) peaks at incident angles of (b) 0.1–1°, (c) 1–3°, and (d) 3–10°.

In our previous study [6], three sub-peaks corresponding to the compressed zone, transition zone (similar to unstrained matrix), and expansion zone were used to fit the S-GIXRD data for low-energy (100 eV) He-ion-irradiated W. In the present case of high-energy He irradiation, however, the S-GIXRD patterns are much more complex and cannot be accurately analyzed by the three sub-peaks model. Here, a new method is proposed to handle the above-mentioned complexity of the present S-GIXRD data.

The penetration depth (D_w) refers to the depth at which the intensity of the incident X-rays (I_0) decays to $1/e$, so the intensity diffracted from a layer at a depth larger than $5D_w$ is negligible, and the S-GIXRD pattern was contributed to dominantly from the subsurface in the range of 0 to $5D_w$. To be accurate enough and to consider the complexity of the fitting software, one divides such a range into 20 equal parts, as shown in Figure 3a, and the diffraction intensity of each part can be approximated by the classical Pseudo-Voigt function:

$$f(h, d) = \frac{r}{1 + g(h - d^{-1})^2} + (1 - r)e^{-C_1 g(h - d^{-1})^2}, \quad (2)$$

where $h = 2\sin\theta/\lambda$ in a unit of $1/\text{nm}$, d is the interplaner spacing, $C_1 = 0.6931$ is a constant, r is the Lorentzian component, and g is the parameter related to profile asymmetry.

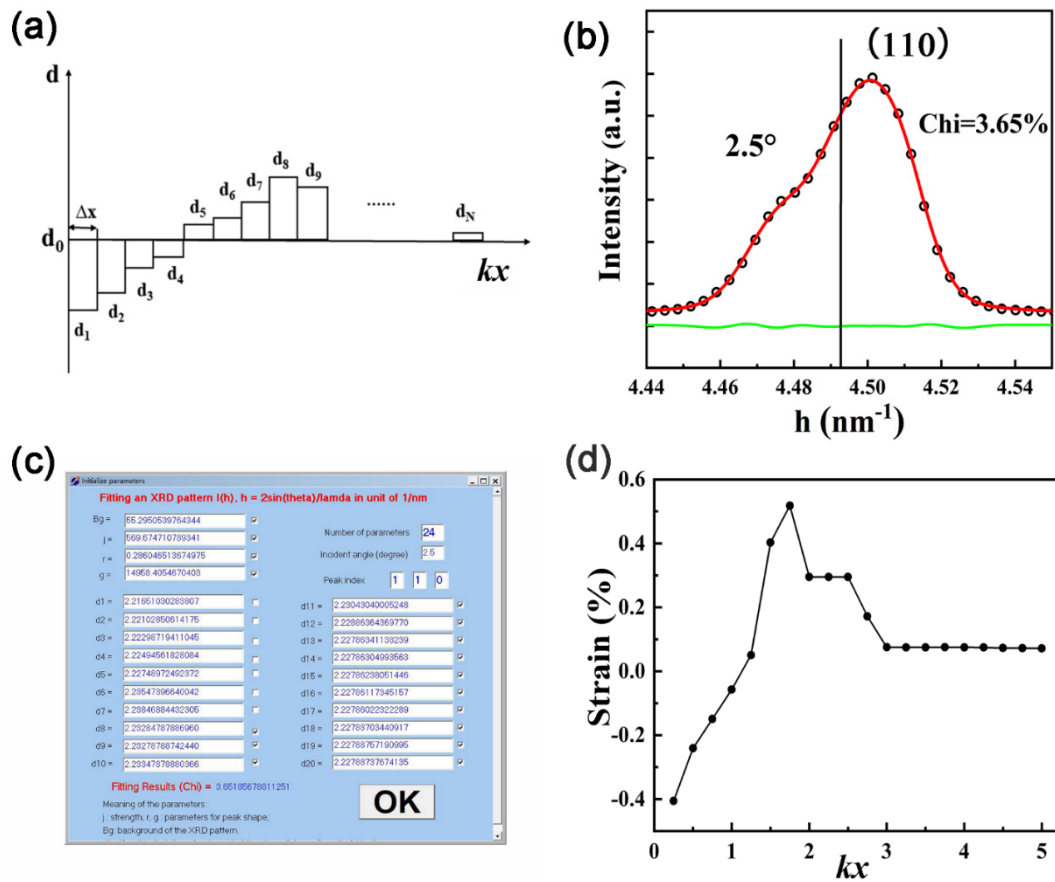


Figure 3. (a) Schematic distribution of interplaner spacing. (b) The fitting result of (110) peak at an incident angle of 2.5° . (c) Fitting parameters in the program at an incident angle of 2.5° . (d) The strain-depth (kx) profile obtained from the fitting.

The integral of X-ray diffraction over the entire depth (I) can be expressed as:

$$I = B_g + \int I_0 e^{-kx} f(h, d) dx, \quad (3)$$

where B_g is the background diffraction, and k is the reciprocal of penetration depth. Since the considered depth range is $0-5 D_w$ and divided into 20 parts, the integral in Equation (3) can be calculated by the following summation:

$$I = B_g + I_0 \Delta x \sum_{i=1}^{20} e^{-(i-0.5)k\Delta x} f(h, d_i), \quad (4)$$

where $\Delta x = D_w/4$, and d_i is the (110) interplaner spacing of the parts at a depth of $(i-0.5)\Delta x$ ($i = 1, 2, \dots, 20$). According to Equation (4), the S-GIXRD data at different incident angles can be well fitted, and the values of the interplaner spacing (d_i) can be obtained. As an example, the fitting result of the (110) peak at an incident angle of 2.5° is shown in Figure 3b, and the corresponding fitting parameters in the program are shown in Figure 3c.

Assuming that the diffraction peak at an incident angle of 10° is mainly contributed to by the unstrained matrix as shown by the black straight line in Figure 2d, the (110) interplaner spacing of the unstrained W can be calculated as $d_{110} = 2.226 \text{ \AA}$. Then, the strain at different depths can be expressed as:

$$\varepsilon = d_i/d_{110} - 1 \quad (5)$$

The variation of the strain with kx obtained for the incident angle of 2.5° is shown in Figure 3d. It can be seen that, with the increasing kx , the strain increases and then decreases to slightly above 0 and finally remains stable after passing a maximum value of 0.5% at $kx = 2$, which corresponds to a depth of $2D_w$ (~574 nm).

To make the strain–depth profile more accurate, the (110) diffraction peaks corresponding to all 13 incident angles were fitted, and the d_i ($i = 1, 2, \dots, 20$) that can be obtained are shown in Table 1. From these parameters, the strains can be calculated using Equation (5) and are shown in Figure 4a. By averaging all calculated strain data, the final strain–depth profile is obtained as the red curve in Figure 4a. It can be seen that, with increasing depth, the strain increases firstly and then decreases to slightly above 0 and finally remains stable after reaching a maximum of about 0.15% at 600 nm. At depths of 0–100 nm, the strain is compressive due to mechanical polishing, while, when the depth exceeds 100 nm, an expansion strain appears which was caused by irradiation-induced lattice swelling.

Table 1. Fitted (110) interplaner spacing d_i of a 2×10^{21} ions/m² irradiated W at different incident angles. Chi represents the fitting error.

d_i (Å)	Incident Angles (°)												
	0.1	0.2	0.3	0.5	1	1.5	2	2.5	3	4	5	7	10
d_1	2.208	2.208	2.208	2.209	2.212	2.217	2.216	2.217	2.219	2.224	2.223	2.224	2.223
d_2	2.208	2.208	2.211	2.214	2.217	2.217	2.219	2.221	2.224	2.224	2.223	2.224	2.226
d_3	2.208	2.212	2.215	2.217	2.217	2.217	2.222	2.223	2.224	2.224	2.230	2.226	2.230
d_4	2.210	2.216	2.215	2.219	2.224	2.217	2.226	2.225	2.224	2.224	2.235	2.233	2.226
d_5	2.214	2.216	2.219	2.224	2.224	2.232	2.227	2.227	2.227	2.234	2.227	2.226	2.226
d_6	2.214	2.219	2.222	2.227	2.224	2.234	2.235	2.235	2.235	2.234	2.227	2.226	2.226
d_7	2.219	2.222	2.223	2.232	2.233	2.233	2.235	2.238	2.235	2.234	2.226	2.226	2.226
d_8	2.222	2.225	2.226	2.231	2.233	2.226	2.235	2.233	2.235	2.227	2.226	2.226	2.226
d_9	2.222	2.225	2.228	2.231	2.233	2.226	2.235	2.233	2.235	2.227	2.226	2.226	2.226
d_{10}	2.225	2.225	2.228	2.224	2.233	2.226	2.233	2.233	2.230	2.227	2.226	2.226	2.226
d_{11}	2.228	2.229	2.228	2.223	2.233	2.226	2.229	2.230	2.228	2.227	2.226	2.226	2.226
d_{12}	2.228	2.229	2.228	2.224	2.233	2.226	2.229	2.228	2.228	2.227	2.226	2.226	2.226
d_{13}	2.228	2.230	2.228	2.224	2.233	2.226	2.229	2.228	2.228	2.227	2.226	2.226	2.226
d_{14}	2.228	2.230	2.230	2.224	2.233	2.226	2.227	2.228	2.228	2.227	2.226	2.226	2.226
d_{15}	2.228	2.230	2.230	2.223	2.224	2.226	2.227	2.228	2.228	2.227	2.226	2.226	2.226
d_{16}	2.228	2.230	2.230	2.223	2.224	2.226	2.227	2.228	2.228	2.227	2.226	2.226	2.226
d_{17}	2.228	2.230	2.232	2.223	2.224	2.226	2.227	2.228	2.228	2.227	2.226	2.226	2.226
d_{18}	2.228	2.230	2.232	2.223	2.224	2.226	2.227	2.228	2.228	2.227	2.226	2.226	2.226
d_{19}	2.228	2.231	2.232	2.223	2.224	2.226	2.227	2.228	2.228	2.227	2.226	2.226	2.226
d_{20}	2.229	2.231	2.232	2.223	2.224	2.226	2.227	2.228	2.228	2.227	2.226	2.226	2.226
Chi (%)	0.77	1.01	0.99	1.28	5.28	5.37	4.35	3.65	3.43	3.31	4.24	3.13	0.33

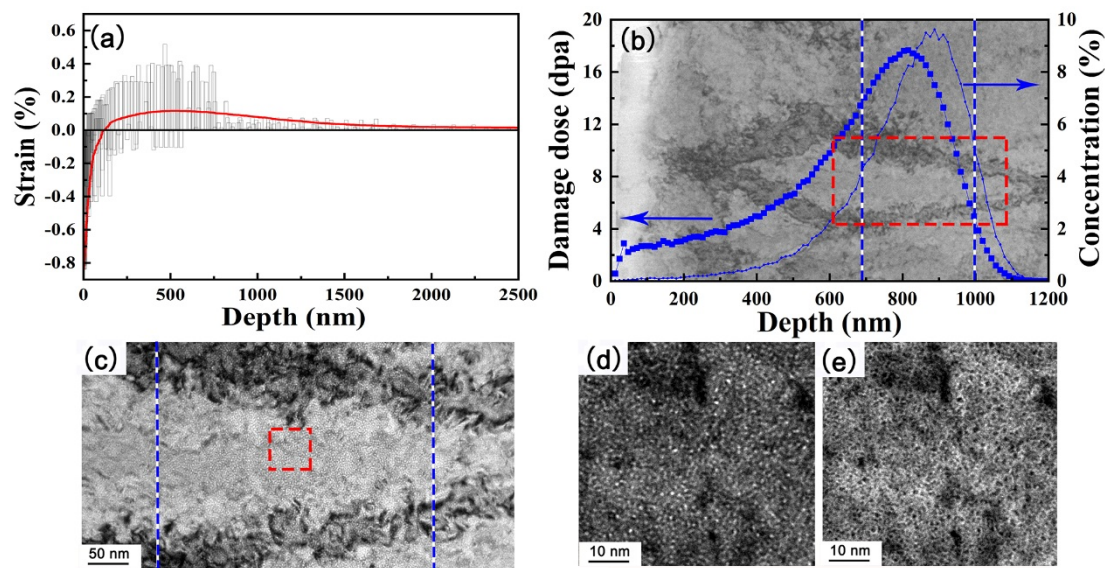


Figure 4. (a) Strain–depth profile at all 13 incident angles. (b) TEM image superposed with a SRIM simulation under 2×10^{21} He ions/cm² irradiation. (c) Enlarged TEM images in the range of 600–1100 nm. (d) Under-focused and (e) over-focused enlarged TEM images in the range of 800–860 nm.

It is worth noting that the variations at each specific depth, where compression and expansion strains can be identified simultaneously, mainly result from fitting errors when fitting the GIXRD with different incident angles. The contribution for GIXRD peaks at low incident angles mainly comes from the surface layer (Figure 2b), which leads to inaccurate calculations of the strain at higher depths, and vice versa for high incident angles. In addition, the location at higher depths can only be detected significantly when the incident angle is relatively high, but at this point the detected signal tends to come from the strain-free matrix, and thus it is reasonable that the calculated strain is almost 0 at higher depths, even though there is only a limited number of data points.

The TEM image superposed with a SRIM simulation under 2×10^{21} He ions/cm² irradiation is presented in Figure 4b, where the maxima of the dpa and He concentration appear at 750–900 nm. It was observed by TEM that helium bubbles with high density and small size (~1 nm) were detected at a distance of about 680 nm from the surface (Figure 4c–e). The helium bubble distribution area was 680–1000 nm. The corresponding displacement per atom (dpa) and the atomic concentration of He versus the depth from the sample surface were calculated by SRIM 2010 full-damage cascade simulations and are also shown in Figure 4b. The fitting settings for energy and fluence were 400 keV and 2×10^{21} ions/m², respectively. It can be seen that the helium bubble distribution and the strain–depth profile obtained from the GIXRD analysis are in good agreement with the dpa and He concentration profile simulated by SRIM. It is worth pointing out that the actual damage region may be wider than that predicted by SRIM, owing to the atomic diffusion at the actual irradiation temperature. In this sense, the strain–depth profile obtained by fitting the S-GIXRD data is reasonable.

4. Conclusions

A new method for analyzing S-GIXRD data at different incident angles for high-energy He-irradiated W was suggested, by which the complex peak shape induced by ion irradiation can be well fitted. For 2×10^{21} He ions/m² irradiated W, in addition to a compressive strain, which exists in the depths of 0–100 nm due to mechanical polishing, an expansion strain appears in the depth exceeds 100 nm, which was caused by irradiation-induced lattice swelling. The strain–depth profile is in good agreement with the dpa and

He concentration profile simulated by the SRIM. This work provides a reference for the study of irradiation damage in the subsurface of W alloys by fitting GIXRD data.

Author Contributions: Conceptualization, M.S. and Q.F.; methodology, W.W. and J.Y.; validation, Z.X.; formal analysis, R.L. and X.W. (Xianping Wang); resources, J.Y., X.W. (Xuebang Wu) and Q.F.; data curation, W.H.; writing—original draft preparation, W.H.; writing—review and editing, M.S.; supervision, Q.F.; project administration, Q.F. and C.L.; funding acquisition, M.S. and Q.F. All authors have read and agreed to the published version of the manuscript.

Funding: This work is subsidized by the National Key Research and Development Program of China (No. 2017YFA0402800, 2017YFE0300402) and the National Natural Science Foundation of China (Grant Nos. 51971213, 52173303, 52101159, 51801203).

Institutional Review Board Statement: Not applicable.

Informed Consent Statement: Not applicable.

Data Availability Statement: Not applicable.

Acknowledgments: The authors thank the BL14B1 stations of SSRF for providing the beam time.

Conflicts of Interest: The authors declare no conflict of interest.

References

1. Villari, R.; Barabash, V.; Escourbiac, F.; Ferrand, L.; Hirai, T.; Komarov, V.; Loughlin, M.; Merola, M.; Moro, F.; Petrizzi, L.; et al. Nuclear analysis of the ITER full-tungsten divertor. *Fus. Eng. Des.* **2013**, *88*, 2006–2010. [[CrossRef](#)]
2. Raffray, A.R.; Nygren, R.; Whyte, D.G.; Abdel-Khalik, S.; Doerner, R.; Escourbiac, F.; Evans, T.; Goldston, R.J.; Hoelzer, D.T.; Konishi, S.; et al. High heat flux components—Readiness to proceed from near term fusion systems to power plants. *Fus. Eng. Des.* **2010**, *85*, 93–108. [[CrossRef](#)]
3. Kim, H.; Kwon, J.; Chang, K. Effect of the Surface Roughness of Tungsten on the Sputtering Yield under Helium Irradiation: A Molecular Dynamics Study. *Metals* **2021**, *11*, 1532. [[CrossRef](#)]
4. Tsuchida, K.; Miyazawa, T.; Hasegawa, A.; Nogami, S.; Fukuda, M. Recrystallization behavior of hot-rolled pure tungsten and its alloy plates during high-temperature annealing. *Nucl. Mater. Energy* **2018**, *15*, 158–163. [[CrossRef](#)]
5. El-Atwani, O.; Hinks, J.A.; Greaves, G.; Gonderman, S.; Qiu, T.; Efe, M.; Allain, J.P. In-situ TEM observation of the response of ultrafine-and nanocrystalline-grained tungsten to extreme irradiation environments. *Sci. Rep.* **2014**, *4*, 4716. [[CrossRef](#)] [[PubMed](#)]
6. Huang, W.J.; Sun, M.; Yang, J.F.; Wen, W.; Xie, Z.M.; Zhang, L.C.; Liu, R.; Chen, C.A.; Jiang, Y.; Wang, X.P.; et al. Microstructure evolution of pure tungsten after low-energy and high-fluence He⁺ implantation assessed by synchrotron grazing incidence X-ray diffraction. *J. Nucl. Mater.* **2021**, *544*, 152663. [[CrossRef](#)]
7. Kötschau, I.M.; Schock, H.W. Depth profile of the lattice constant of the Cu-poor surface layer in (Cu₂Se)_{1-x}(In₂Se₃)_x evidenced by grazing incidence X-ray diffraction. *J. Phys. Chem. Solids* **2003**, *64*, 1559–1563. [[CrossRef](#)]
8. Chen, Z.; Han, W.; Yu, J.; Zhu, K. Effect of 800 keV argon ions pre-damage on the helium blister formation of tungsten exposed to 60 keV helium ions. *J. Nucl. Mater.* **2016**, *472*, 110–117. [[CrossRef](#)]
9. Ipatova, I.; Greaves, G.; Pacheco-Gutiérrez, S.; Middleburgh, S.C.; Rushton, M.J.D.; Jimenez-Melero, E. In-situ TEM investigation of nano-scale helium bubble evolution in tantalum-doped tungsten at 800 °C. *J. Nucl. Mater.* **2021**, *550*, 152910. [[CrossRef](#)]
10. Cunningham, W.S.; Hattar, K.; Zhu, Y.; Edwards, D.J.; Trelewicz, J.R. Suppressing irradiation induced grain growth and defect accumulation in nanocrystalline tungsten through grain boundary doping. *Acta Mater.* **2021**, *206*, 116629. [[CrossRef](#)]
11. Jiang, W.; Zhu, Y.; Zhang, L.; Edwards, D.J.; Overman, N.R.; Nandipati, G.; Setyawan, W.; Henager, C.H., Jr.; Kurtz, R.J. Dose rate effects on damage accumulation and void growth in self-ion irradiated tungsten. *J. Nucl. Mater.* **2021**, *550*, 152905. [[CrossRef](#)]
12. Demir, E.; Mirzayev, M.N.; Popov, E.P.; Horodek, P.; Genov, I.G.; Siemek, K.; Mirzayeva, D.M.; Turchenko, V.A.; Bulavin, M.; Beskrovnyi, A.I.; et al. Effects of high-energetic 3He⁺ ion irradiation on tungsten-based composites. *Vacuum* **2021**, *184*, 109934. [[CrossRef](#)]
13. Baklanov, V.; Zhanbolatova, G.; Skakov, M.; Miniyazov, A.; Sokolov, I.; Tulenbergenov, T.; Kozhakhmetov, Y.; Bukina, O.; Orazgaliev, N. Study of the temperature dependence of a carbided layer formation on the tungsten surface under plasma irradiation. *Mater. Res. Express* **2022**, *9*, 16403. [[CrossRef](#)]
14. Deng, H.W.; Xie, Z.M.; Wang, Y.K.; Liu, R.; Zhang, T.; Hao, T.; Wang, X.P.; Fang, Q.F.; Liu, C.S. Mechanical properties and thermal stability of pure W and W-0.5 wt% ZrC alloy manufactured with the same technology. *Mater. Sci. Eng. A* **2018**, *715*, 117–125. [[CrossRef](#)]
15. Dutta, A.; Das, K.; Gayathri, N.; Menon, R.; Nabhiraj, P.Y.; Mukherjee, P. Effect of Ar⁹⁺ irradiation on Zr-1Nb-1Sn-0.1 Fe alloy characterized by Grazing Incidence X-ray diffraction technique. *Phys. Chem.* **2018**, *144*, 125–131.
16. Hubbell, J.H.; Seltzer, S.M. *Tables of X-ray Mass Attenuation Coefficients and Mass Energy-Absorption Coefficients 1 keV to 20 MeV for Elements z = 1 to 92 and 48 Additional Substances of Dosimetric Interest*; National Institute of Standards and Technology—PL: Gaithersburg, MD, USA, 1995.